

Two distinct immunopathological profiles in autopsy lungs of COVID-19

Short title: Profiles of COVID-19 autopsy lungs

Ronny Nienhold^{1§}, Yari Ciani^{2§}, Viktor H. Koelzer^{3,4§}, Alexandar Tzankov⁵, Jasmin D. Haslbauer⁵, Thomas Menter⁵, Nathalie Schwab¹, Maurice Henkel¹, Angela Frank¹, Veronika Zsikla¹, Niels Willi¹, Werner Kempf⁶, Thomas Hoyle⁷, Mattia Barbareschi⁸, Holger Moch³, Markus Tolnay⁵, Gieri Cathomas¹, Francesca Demichelis^{2,9*}, Tobias Junt^{7*}, Kirsten D. Mertz^{1*}

Affiliations:

¹ Institute of Pathology, Cantonal Hospital Baselland, Liestal, Switzerland

² Laboratory of Computational and Functional Oncology, Department for Cellular, Computational and Integrative Biology – CIBIO, University of Trento, Trento, Italy

³ Department of Pathology and Molecular Pathology, University Hospital Zurich, Zurich, Switzerland

⁴ Department of Oncology and Nuffield Department of Medicine, University of Oxford, Oxford, United Kingdom

⁵ Pathology, Institute of Medical Genetics and Pathology, University Hospital Basel, Basel, Switzerland

⁶ Kempf und Pfaltz Histologische Diagnostik, Zurich, Switzerland

⁷ Novartis Institutes for BioMedical Research (NIBR), Basel, Switzerland

⁸ Anatomia ed Istologia Patologica, Ospedale S. Chiara di Trento, Trento, Italy

⁹ Caryl and Israel Englander Institute for Precision Medicine, Institute for Computational Biomedicine, New York Presbyterian Hospital, Weill Cornell Medicine, New York, New York, USA

§ These authors jointly contributed to this work.

* These authors jointly directed this work.

Word count: Abstract 168 / Main text 3541 (Introduction, Results, Discussion)

Correspondence:

PD Dr. med. Kirsten D. Mertz, MD PhD

Institute of Pathology Liestal

Cantonal Hospital Baselland

Mühlemattstrasse 11

CH-4410 Liestal, Switzerland

Phone: + 41 (0) 61 925 2635

Email: kirsten.mertz@ksbl.ch

Abstract

Coronavirus Disease 19 (COVID-19) is a respiratory disease caused by severe acute respiratory syndrome coronavirus 2 (SARS-CoV-2), which has grown to a worldwide pandemic with substantial mortality. Immune mediated damage has been proposed as a pathogenic factor, but immune responses in lungs of COVID-19 patients remain poorly characterized. Therefore we conducted transcriptomic, histologic and cellular profiling of *post mortem* COVID-19 (n=34 tissues from 16 patients) and normal lung tissues (n=9 tissues from 6 patients). Two distinct immunopathological reaction patterns of lethal COVID-19 were identified. One pattern showed high local expression of interferon stimulated genes (ISG^{high}) and cytokines, high viral loads and limited pulmonary damage, the other pattern showed severely damaged lungs, low ISGs (ISG^{low}), low viral loads and abundant infiltrating activated CD8+ T cells and macrophages. ISG^{high} patients died significantly earlier after hospitalization than ISG^{low} patients. Our study may point to distinct stages of progression of COVID-19 lung disease and highlights the need for peripheral blood biomarkers that inform about patient lung status and guide treatment.

Introduction

COVID-19 is a pandemic respiratory disease with 2-3% lethality and a particularly severe course in males, patients with cardiovascular comorbidities and in the elderly^{1,2}. Lymphopenia, high levels of pro-inflammatory cytokines in the circulation³, and phenotypic changes of pro-inflammatory macrophages in bronchoalveolar lavages⁴ in severe patients have led to the notion that the immune response against the causative virus SARS-CoV-2 may contribute to devastating end organ damage⁵. Since patients with severe COVID-19 may develop acute respiratory distress syndrome (ARDS) and many patients die from respiratory failure with diffuse alveolar damage⁶, it is critical to understand the immunological profiles in the lungs of these patients.

To better understand the molecular and cellular underpinnings of COVID-19 lung disease, we used histologic and transcriptional analyses of *post mortem* lung tissues in a cohort of patients where the cause of death was respiratory failure. We detected two distinct immunological and cellular profiles in the lungs of these patients, defined by their differential expression of interferon stimulated genes (ISGs) and immune infiltration patterns, which we termed ISG^{high} and ISG^{low}. ISG subgroups strongly differed in regards to the characteristics and the extent of pulmonary damage, pulmonary viral loads, disease course and time to death from hospitalization. These data highlight two distinct patterns of immune pathology of pulmonary COVID-19 and may give insight into the natural progression of COVID-19 in lungs.

Results

Two patterns of gene expression in COVID-19 autopsy lungs

Here we analyzed 34 *post mortem* lung samples from 16 deceased COVID-19 patients and 9 *post mortem* lung samples from 6 patients, who died from non-infectious causes (**Table 1**). The primary cause of death in all patients of this cohort was respiratory failure, sometimes multi-organ failure including failure of the respiratory system. Since lung samples from the same patients did not always appear morphologically uniform, all lung specimens were subjected to differential gene expression analysis based on a commercially available targeted next generation sequencing (NGS) assay (OIRRA) designed for quantification of immune cell and inflammatory transcripts (**Supplementary Table 2**). Among the 398 genes investigated, we identified 68 up-regulated and 30 down-regulated genes in COVID-19 infected lungs compared to normal tissue (**Figure 1a,b**; **Supplementary Table 3**), and a PCA analysis showed segregation of COVID-19 patients in two well-defined clusters that showed distinct association with viral load (**Figure 1a,c**).

Using a consensus of 30 different indices⁷ we identified three groups of samples defined by distinct expression levels of the deregulated genes by K-means clustering (**Figure 1a**). Clusters 1 (50% of samples) and 2 (41%) contained COVID-19 samples while cluster 3 contained all normal lung samples as well as three COVID-19 samples (9%). To understand why the majority of COVID-19 lung tissues segregated into defined clusters 1 or 2, we undertook a gene ontology analysis. We identified ISGs as a key upregulated pathway in COVID-19 autopsy lungs (**Table 2**), which was differentially represented in cluster 1 and 2, respectively (**Figure 1d**). Identification of an ISG^{high} cluster (Cluster 1, ISG^{high}) was surprising, since SARS-CoV-2 was recently proposed to lead to limited ISG induction, yet only in comparison to other respiratory viruses⁸. Our data suggest that autopsy lungs of COVID-19 patients, who died from respiratory failure, showed two different gene expression patterns with different levels of ISG activation (ISG^{high} and ISG^{low}).

Clinical differences of COVID-19 patients with an ISG^{high} versus ISG^{low} lung profile

Patients, whose lung samples all segregated in the ISG^{high} or in the ISG^{low} subgroups, were called ISG^{high} and ISG^{low} patients. To investigate whether there were clinical differences between these two patient groups, we compared their clinical and epidemiological information. The majority of COVID-19 patients in our cohort (81%) were male and the average body mass index (BMI) was 31.4. kg/m². Patient level analysis revealed no correlation of sex or BMI with the ISG patterns (**Figure 1a**). All patients in our cohort died from respiratory failure or multi-organ failure including failure of the respiratory system, independent of ISG subgrouping. When we analysed comorbidities and autopsy findings, we found that 5 out of 7 (71%) ISG^{low} patients, but none of the ISG^{high} patients had an autopsic finding of a thromboembolic event in the lungs and/or disseminated intravascular dissemination (DIC) indicating an abnormally activated blood coagulation (hypercoagulability) exclusively in ISG^{low} patients. COVID-19 associated coagulopathy was unlikely to contribute to rapid exacerbation of pulmonary COVID-19 since this diagnostic criterion was only observed in patients displaying the ISG^{low} phenotype. Most notably, when we compared the disease course and hospitalization time between the patients with different ISG lung profiles, we found a significantly longer hospitalization time for ISG^{low} patients from admission to death compared to ISG^{high} patients (**Figure 1e**). Of note, we did not find differences in the anamnestic onset of disease symptoms and time from positive testing for COVID-19 infection by nasopharyngeal swab to hospitalization or death between ISG^{high} and ISG^{low} patients. To exclude bacterial and viral superinfections as a confounder of clinical course, we performed whole genome sequencing on all samples to detect bacterial and/or viral DNA. Bacterial superinfections were found in three lung tissue samples, in 3/16 COVID-19 patients, that were equally distributed among the different groups (**Figure 2a-e**).

Based on the limited number of samples with evidence of bacterial superinfection, there was no correlation with clinical subgroups or the duration of the disease.

Taken together, expression of the ISG^{high} profile in COVID-19 lungs is associated with accelerated disease course and early lethal outcome. The ISG^{low} profile is associated with coagulopathies and later lethal outcome. This points to two distinct clinical courses of fatal COVID-19 pulmonary disease. Since autopsy studies always focus on disease endpoints, our data do not allow us to draw direct conclusions about natural stages of disease progression in COVID-19 lungs. However, it is very suggestive that the ISG^{high} profile precedes the ISG^{low} profile, consistent with a longitudinal study in peripheral blood showing that ISG expression was high in early COVID-19 and declined later⁹.

Immune microenvironment characteristics of the ISG^{high} and ISG^{low} COVID-19 lung profiles

In line with a recent study showing a correlation of ISG expression and viral load in nasopharyngeal swabs¹⁰, expression of ISGs was positively correlated with pulmonary viral load (**Figure 3a**), and immunohistochemical staining confirmed the presence of SARS-CoV-2 nucleocapsid protein in ISG^{high} lungs, mainly localized to pneumocytes (**Figure 3b**).

SARS-CoV-2 induces a strong antiviral immune response. Therefore we analysed frequencies of specific immune cells in lungs by computational image analysis. T cells (CD3+) of the CD4+ and CD8+ lineages, B cells (CD20+), and macrophages (CD68+) were selectively enriched in lung tissues from ISG^{low} patients (**Figure 3c,d; Figure 4a,b**). A strong enrichment for CD68+ and CD163+ monocytes in lung tissue was observed with spatial correlation of stains for both markers indicating co-expression. Since circulating monocytes in COVID-19 patients co-express CD68 and CD163, it was not surprising that CD68 and CD163 expression in lungs followed a similar pattern¹¹ (**Figure 3c,d**). Surprisingly, CD123+ plasmacytoid dendritic cells (pDCs) did not show elevated frequencies in ISG^{high} lungs (**Figure 4a,b**), and the type 1 IFN (IFN-I) genes that we measured (IFNa17, IFNb1) were not higher expressed in ISG^{high} lungs with high viral load compared to ISG^{low} lungs (*data not shown*), potentially because SARS-CoV-2 inhibits IFN-I production⁸. Therefore our analysis did not allow us to identify the upstream trigger of ISGs in lungs.

A cytokine storm has been proposed to cause adverse outcome of COVID-19¹². It has been suggested that peripheral monocytes do not contribute to it¹³, yet cytokines are highly expressed in bronchoalveolar lavages (BALs) of COVID-19 patients⁴. Therefore we investigated expression of a

pro-inflammatory cytokine signature (TNF, IL1B, IL6, CCL2, IFNA17, IFNB1, CXCL9, CXCL10, CXCL11) in lung samples from lethal COVID-19. The proinflammatory gene signature was significantly enriched in the ISG^{high} subset ($p=0.0061$) (**Figure 5a**). Activated CD8+ T cells are essential for elimination of coronaviruses^{14,15}. Therefore we defined and investigated an activated cytotoxic T cell signature (CD38, GZMA, GZMB, CCR5) and found that it was inversely correlated to viral counts, particularly in ISG^{low} cases (**Figure 5b**). This suggests that activated CD8+ T cells may indeed contribute to the elimination of SARS-CoV-2 in lungs.

Taken together these data show that COVID-19 autopsy lungs with an ISG^{high} profile show high virus titers, high local expression of innate cytokines and weak immune cell infiltration, while COVID-19 lungs with an ISG^{low} profile show low virus titers, lower expression of innate cytokines and strong immune cell infiltration. This pattern could indicate expression of the lung ISG^{high} profile at an earlier, innate disease stage, i.e. at a time when the virus is not yet controlled, and expression of the ISG^{low} profile at a later disease stage, i.e. after T cell priming.

The ISG^{high} and ISG^{low} lung immunoprofiles correlate with morphological changes

To investigate the potential immunological causes for lung damage in COVID-19, we studied whether ISG profiles in COVID-19 *post mortem* lungs were associated with specific histomorphological features of fatal COVID-19. Diffuse alveolar damage (DAD) was mostly found in ISG^{low} patients (**Figure 5c**), but intra-alveolar hemorrhage (IAH) was not associated with lung ISG status.

As the cytokine storm was implicated in decline of COVID-19 patients, we analysed whether expression of the above defined pro-inflammatory cytokine signature was associated with IAH but this was not the case (**Figure 5d**). However, within this cytokine signature we identified co-regulated subgroups (IL1B/IL6/TNF, IFNB1/IFNA17, CCL2/CXCL9/CXCL10/CXCL11) (**Figure 5e**). Of these, the CXCL9/10/11 sub-signature was positively associated with IAH (**Figure 5f-i**). This is in line with observations that these chemokines compromise endothelial integrity via CXCR3¹⁶, and that CXCL10 is a key determinant of severe COVID-19¹⁷. Interestingly, basal levels of CXCL9 or CXCL10 are elevated in elderly, hypertensive and obese individuals, who were strongly represented in our autopsy cohort (**Table 1**) and are predisposed to severe COVID-19^{18,19}.

It has been proposed that infiltrating monocytes and macrophages play a role in lung damage^{4,20}. In support of this data, we found CD68+ macrophage infiltrates to be positively associated with DAD (**Figure 5j**). In addition, DAD was associated with the activated cytotoxic T cell signature ($p=0.0022$) (**Figure 5k**), yet not with the overall numbers of pulmonary CD8+ T-cells (**Figure 5l**). This raises the

possibility that activated CD8+ T cells contribute to DAD as they eliminate virus from infected lungs. None of the above pulmonary cytokine sub-signatures, however, was positively associated with DAD (**Figure 5m-p**), suggesting that none of these cytokines drives lung pathology directly.

In summary, we did not find distinct features of lung damage in ISG^{high} patients, suggesting that extra-pulmonary factors may contribute to mortality in these patients. However, ISG^{low} patients show prominent DAD, associated with peri-alveolar foci of CD68+ macrophages and an activated T cell signature. Local expression of most cytokines did not correlate to lung damage, except for CXCL9/10/11, which correlated to IAH (p=0.018) (**Figure 5i**). Based on studies that associated serum CXCL10 levels with general disease severity¹⁷, it will be interesting to investigate whether serum levels of these cytokines predict a specific pattern of lung damage.

The ISG^{low} lung profile shows signs of tissue regeneration and T cell exhaustion

Since ISG^{low} lung samples were derived from patients with a longer disease course, we investigated specific pathways of local immune regulation and tissue regeneration. ISG^{low} lung samples expressed elevated p53 and Ki67 (**Figure 1a, Figure 6a**), i.e. reactive markers indicating lung remodeling in DAD²¹.

Since we found local upregulation of C1QA (p=0.017) and C1QB (p=0.0012) specifically in ISG^{low} lungs (**Figure 1a, Figure 6b**), we hypothesized that complement activation may further contribute to lung damage in these patients. Consistently, we found strong staining for C3d and C5b-9 complex deposition in lung tissue indicating complement activation in lungs of ISG^{low} patients (**Figure 6c**). Since C1Q also restrains antiviral CD8+ effector T cell responses²², it may contribute to the local regulation of effector T cells. In line with previous observations²³, we found a higher frequency of CD8+PD1+ T-cells in the ISG^{low} subgroup (p=0.001), potentially indicative of T cell exhaustion (**Figure 4a,b**).

Overall our results identify two patterns of pulmonary COVID-19 disease that lead to death from respiratory failure. Patients of the ISG^{high} subgroup die early with high viral loads and high cytokine and ISG expression levels in lungs. Their lungs are morphologically relatively intact, and our data do not identify a uniform pathomechanism underlying lethal outcome, although some show CXCL9/10/11-associated IAH (**Figure 5i**). The distinct ISG^{low} group of patients dies later, with low viral loads in the lungs, low local expression of cytokines and ISGs, yet strong infiltration of pulmonary tissue by CD8+ T cells and macrophages, which both correlate to severity of DAD and local complement activation. Some of these patients show IAH in addition to DAD, and many of them suffer from coagulopathies. Altogether this patient group appears to suffer from severe

pulmonary immunopathology. The design of our autopsy study does not allow to directly conclude that ISG^{low} lungs might have undergone a previous ISG^{high} phase, though circumstantial evidence about the general course of coronavirus infections may suggest this possibility.

Discussion

Here we describe two immunopathological patterns in lungs of fatal COVID-19 patients based on ISG expression. The ISG^{high} pattern is observed in patients, who die early after hospitalization and is characterized by high viral load and high levels of pro-inflammatory cytokines, yet relatively intact lung morphology, while the ISG^{low} pattern is characterized by low viral load, massive lung damage, marked lung immune cell infiltrates and late death. Our findings are consistent with epidemiological data showing two peaks of mortality²⁴, and another study of four COVID-19 autopsies, where one patient died early after hospital admission, with striking upregulation of pulmonary IL-1b/IL-6 in lungs and little lung damage, while three patients expressed low levels of pulmonary cytokines, massive DAD and delayed death²⁵. Therefore our study allows us to propose two immunopathological stages of pulmonary COVID-19.

The segregation of autopsy lung samples from COVID-19 patients in two groups based on ISG expression contributes to our understanding of the interferon response against SARS-CoV-2. Like other coronaviruses, SARS-CoV-2 is particularly sensitive to type I interferons^{8,26}. Therefore, and similar to other coronaviruses²⁷, it has evolved strategies to evade the interferon response, and SARS-CoV-2 leads to relatively weak IFN-I/III release in host cells at low multiplicities of infection⁸. This initial delay of IFN-I/III production may facilitate initial virus replication in lungs, as studies with SARS-CoV in mice have shown, and enable an eventual increase of the IFN-I response and death¹⁵. A similar observation was made for fatal SARS-CoV infections in humans, which were accompanied by elevated expression of ISGs²⁸. Since the SARS-CoV-2 receptor ACE2 is itself an ISG on lung epithelial cells²⁹, virus infection and the interferon response may promote each other in this phase of the infection. This may explain the observed correlation of high ISG expression and high viral load in lungs and widespread presence of SARS-CoV-2 in lung epithelial cells. Together this may contribute to fatal outcome of SARS-CoV-2 infections in the ISG^{high} group.

The observation of the ISG^{high} pattern in COVID-19 autopsy lungs seems to be at odds with initial observations that critical COVID-19 patients express on average lower ISGs in blood than patients with a milder course of disease³⁰. One possible explanation is that the blood ISG status is not directly reflective of the lung. In support of this idea, bronchoalveolar lavages (BALs) from

severe/critical patients showed high proportions of ISG^{high} macrophages and high expression of CXCL9/10/11, IL6, IL-1b, TNF, CCL2⁴, which is reflective of our ISG^{high} phenotype in lung autopsies. An alternative explanation for the apparent disconnect of lung and blood ISG status may come from the overall frequency of the ISG^{high} subtype of critical/fatal COVID-19: ISGs are highly expressed in blood of COVID-19 patients during the early, innate phase of COVID-19⁹, and we show that patients with an ISG^{high} status in lungs die early upon hospitalization. While the early-mortality subset accounted for 44% of all deaths in our study, epidemiological data from France²⁴ suggest that this early critical subset is actually smaller: only 15% of patients died early after hospitalization. This percentage is consistent with the study by Hadjadj *et al.*, which detects high ISG expression in blood of 3/17 (18%) critical COVID-19 patients, yet this signal gets diluted in the majority of ISG^{low} critical cases³⁰. These two alternative explanations show how critical it will be to compare gene expression in blood and lungs of individual patients at different times of the infection and to identify peripheral biomarkers for COVID-19 lung status.

ISG^{low} COVID-19 patients in our study die with classical features of DAD³¹, on average 9.1 days after hospitalization. Later death compared to patients with an ISG^{high} pattern and progressive decline of systemic ISG expression during COVID-19^{9,13} led us to infer that the ISG^{low} pattern in lungs reflects a later phase of pulmonary COVID-19. ISG^{low} lungs show higher frequencies of T and B lymphocytes, compared to ISG^{high} lungs. None of our fatal cases showed lung lymphocyte counts below control levels. Therefore COVID-19 associated lymphopenia in blood^{23,32} or spleens³ does not translate into lymphocyte depletion in infected lungs. Potential reasons are that the infected lung acts as a potent sink for circulating lymphocytes and that local proliferation limited recruitment from the blood, as was shown for CD8+ T cells in BAL of severe patients⁴. Consistent with previous observations³³ we describe an activated CD8+ T cell signature in lungs of ISG^{low} patients that contain low viral counts. This suggests that CD8+ T cells are critical for antiviral protection, and may transition into a protective memory pool, as observed for SARS-CoV^{34,35}. In addition, we found elevated frequencies of CD8+PD1+ cells in ISG^{low} lungs compared to ISG^{high} lungs, but not above control levels. The observation that PD-1 levels are elevated in peripheral CD8+ T cells of severe COVID-19 infection, and whether this indicates exhaustion, remains controversial^{13,23}. Overall, although we did not have paired serum antibody levels available, the infiltration pattern of ISG^{low} lungs suggested adaptive immune activation.

While our study sheds further light on COVID-19 lung disease, conclusions on therapy must be drawn with caution. We found that early after hospitalization, ISG^{high} autopsy lungs had uniformly high titers of SARS-CoV-2, and others found that viral loads in swabs and sputum are highest in early COVID-19³⁶. This could indicate that treatment with compounds that directly interfere with the

SARS-CoV-2 replication cycle, e.g. protease or polymerase inhibitors, should start early. However, high expression of ISGs in some lung autopsies raises caution about the use of IFN-I/III as therapeutics, at least as long as causes and consequences of interferon signaling in COVID-19 lungs remain unclear. We found reduced viral counts in ISG^{low} patients, but did not identify the moment at which the body is cleared of the virus. Therefore our findings of reduced viral loads in ISG^{low} patients should not be taken as justification to withhold compounds that directly interfere with the SARS-CoV-2 replication cycle from patients. Extending previous work³⁷, we found signs of elevated complement activation specifically in ISG^{low} lungs. However, it is not known whether complement is synchronously activated in patient lungs and plasma³⁸. Therefore, our results do not provide a further step towards personalized patient care but strengthen the hypothesis that complement inhibitors may show therapeutic benefit, at least in some COVID-19 patients.

Our study has several limitations. The fact that patients with the innate / ISG^{high} stage die early while patients with the lymphocytic / ISG^{low} profile die late after hospitalization, together with knowledge about the immune reaction against other coronaviruses, strongly suggests that COVID-19 lung disease progresses from an ISG^{high} to an ISG^{low} stage. However, an autopsy study is, by design, not longitudinal. Therefore we do not have formal proof that all COVID-19 infected ISG^{low} lungs have undergone a previous ISG^{high} stage. Also, it is unknown why some patients die early and others late. In addition, our focus on the lung only allowed us to investigate pulmonary factors of patient mortality, i.e. an overshooting innate immune activation with IAH in both ISG^{high} and ISG^{low} cases and DAD in ISG^{low} cases. No reported cause of death was enriched in ISG^{high} or ISG^{low} patients, and multi-organ failure was reported as a cause of death only for two of our patients. Another limitation is that we lack gene expression data from blood of autopsy patients or serological data at the time of death. Therefore we were not able to identify peripheral biomarkers predicting specific immunological profiles in the lung. Finally, we analyzed our lungs with a focused gene expression set since quality and quantity of autopsy-derived RNA is often insufficient for unbiased methods. In spite of this technical limitation, which restricted our analysis, we were able to uncover two novel and distinct immunopathological profiles in lungs of fatal COVID-19.

Taken together, our autopsy study sheds light on two distinct courses of lethal COVID-19 in lungs. It remains to be seen whether interferon signaling is only associated with or causally involved in these disease courses. However, our study strengthens the notion that interferon signaling is a central determinant of the pulmonary immune response against SARS-CoV-2.

Methods

Ethics statement

This study was conducted according to the principles expressed in the Declaration of Helsinki. Ethics approval was obtained from the Ethics Committee of Northwestern and Central Switzerland (Project-ID 2020-00629). For all patients, either personal and/or family consent was obtained for autopsy and sample collection.

Patients and sample collection

The study is based on the analysis of 16 out of 21 consecutive COVID-19 autopsies performed between March 9th and April 14th 2020 at the Institute of Pathology Liestal and Institute of Medical Genetics and Pathology Basel, Switzerland. Clinical features including symptoms, course of disease, comorbidities, laboratory results and therapy are listed in **Table 1a**. Detailed autopsy findings for each patient were recently published, and the identifiers (with the prefix “C”) for each COVID-19 patient are consistent with the description of this Swiss COVID-19 autopsy cohort⁶. In this study, we analysed formalin fixed and paraffin embedded (FFPE) lung tissue of distinct areas of the lungs of 16 of these COVID-19 patients. All 16 COVID-19 patients had positive nasopharyngeal swabs collected while alive. In all COVID-19 patients, diagnosis was confirmed by detection of SARS-CoV-2 in postmortal lung tissues. 5/16 patients were additionally tested by postmortal nasopharyngeal swabs which were positive for SARS-CoV-2 in all 5 cases.

As a control cohort, we selected 6 autopsies performed between January 2019 and March 2020 at the Institute of Pathology Liestal (“normal” patients N1 – N6). These control patients died of other, non-infectious causes and had a similar age, gender and cardiovascular risk profile. Patients with infections were excluded from this control cohort. Another control cohort consisted of 4 autopsies of patients suffering from various infections mainly with bacteria affecting the lung (patients with lung pathology, P1 – P4). Details for both control cohorts are listed in **Table 1b,c**. SARS-CoV-2 was ruled out for each control patient by PCR-examination of lung tissue samples.

Nucleic acid extraction

RNA was extracted from up to six sections of FFPE tissue blocks using RecoverAll Total Nucleic Acid Isolation Kit (Cat No. AM1975, Thermo Fisher Scientific, Waltham, MA, USA). Extraction of

DNA from up to 10 sections of FFPE tissue samples was automated by EZ1 Advanced XL (Qiagen, Hilden, Germany) using the EZ1 DNA Tissue Kit (Cat No. 953034, Qiagen, Hilden, Germany). Concentration of DNA and RNA were measured with Qubit 2.0 Fluorometer and Qubit dsDNA HS Assay or Qubit RNA HS Assay (Cat No. Q33230 & Q32852, Thermo Fisher Scientific, Waltham, MA, USA), respectively.

Quantification of SARS-CoV-2 in FFPE tissue samples

Post mortem viral load was individually measured in all lung tissue blocks from all patients included in this study. SARS-CoV-2 was detected in 15ng of human total RNA using the TaqMan 2019-nCoV Assay Kit v1 (Cat No. A47532, Thermo Fisher Scientific, Waltham, MA, USA), which targets three genomic regions (ORF1b, S Protein, N Protein) specific for SARS-CoV-2 and the human RNase P gene (RPPH1). The copy numbers of the SARS-CoV-2 viral genome was determined by utilizing the TaqMan 2019-nCoV Control Kit v1 (Cat No. A47533, Thermo Fisher Scientific, Waltham, MA, USA) and a comparative “ $\Delta\Delta C_T$ ” method. The control kit contains a synthetic sample with a defined amount of target molecules for the human RPPH1 and the three SARS-CoV-2 assays, and was re-analyzed in parallel with patient samples. For each patient sample, this method resulted in individual copy numbers of the human RPPH1 and the three SARS-CoV-2 targets. Finally, the mean copy number of the SARS-CoV-2 targets was normalized to 1×10^6 RPPH1 transcripts.

Profiling of immune response by targeted RNAseq

The expression levels of 398 genes, including genes relevant in innate and adaptive immune response and housekeeping genes for normalization, were analyzed with the Oncomine Immune Response Research Assay (OIRRA, Cat No. A32881, Thermo Fisher Scientific, Waltham, MA, USA). The OIRRA is a targeted gene expression assay designed for the Ion™ next-generation sequencing (NGS) platform. Our study focused on the analysis of rare autopsy tissue samples from COVID-19 patients collected in clinical routine during the COVID-19 pandemic. An inherent problem for transcriptomic studies of autopsy tissues is that it is often not possible to extract high quality RNA in sufficient amounts. To avoid sample dropout due to these reasons, we decided to use a robust and straightforward targeted gene expression assay (OIRRA) rather than whole transcriptome analysis. Since the focus of our study was to investigate the immune profile of lungs, an immunoprofiling assay was deemed most appropriate. The OIRRA gene expression assay was originally designed to interrogate the tumor microenvironment to enable mechanistic studies and identification of predictive biomarkers for immunotherapy in cancer. The assay is optimized to measure the expression of genes involved in immune cell interactions and signaling, including

genes expressed at low levels and involved in inflammatory signaling. The 398 genes covered by this assay are listed in **Supplementary Table 2**. The accessibility of such commercially available assays could be an encouragement to hospitals around the world to conduct similar molecular profiling studies of diagnostic tissue samples from COVID-19 patients, allowing relatively fast and easy stratification of patients into distinct biological groups as a starting point for targeted intervention strategies.

The NGS libraries were prepared as recommended by the supplier. In brief, 30ng of total RNA were used for reverse transcription (SuperScript VILO, Cat No. 11754250, Thermo Fisher Scientific, Waltham, MA, USA) and subsequent library preparation. The libraries were quantified (Ion Library TaqMan Quantitation Kit, Cat No. 4468802, Thermo Fisher Scientific, Waltham, MA, USA), equimolarly pooled and sequenced utilizing the Ion GeneStudio S5xl (Thermo Fisher Scientific, Waltham, MA, USA). De-multiplexing and gene expression level quantification were performed with the standard setting of the ImmuneResponseRNA plugin (version 5.12.0.1) within the Torrent Suite (version 5.12.1), provided as part of the OIRRA by Thermo Fisher Scientific, Waltham, MA, USA.

Detection of co-infections by whole genome sequencing

To identify potential pathogens accompanying an infection with SARS-CoV-2, we analyzed the DNA of the same tissue samples used for detection and profiling of the SARS-CoV-2-specific immune response. First, 250ng of genomic DNA was enzymatically sheared (15 minutes at 37°C) and barcoded using the Ion Xpress Plus Fragment Library Kit (Cat No. 4471269, Thermo Fisher Scientific, Waltham, MA, USA). Subsequently, the libraries were quantified (Ion Library TaqMan Quantitation Kit, Cat No. 4468802, Thermo Fisher Scientific, Waltham, MA, USA) and up to three libraries were pooled at equimolar levels for analysis with Ion GeneStudio S5xl (Thermo Fisher Scientific, Waltham, MA, USA). Sequencing data for each sample was analysed using the CLC genomics workbench (version 20.0.3, Qiagen, Hilden, Germany) in combination with the microbial genomics module (version 20.0.1, Qiagen, Hilden, Germany): The raw reads were trimmed by quality (Mott algorithm with limit 0.05 and a maximum of 2 ambiguous bases per read) and mapped to the human genome (GRCh37 hg19, match score: 1, mismatch cost: 2, indel opening cost: 6, indel extension cost: 1). Unmapped reads were analysed by taxonomic profiling to identify reads of viral or bacterial origin. The profiling utilized an index of 11'540 viral genomes with a minimum length of 1'000 bp and 2'715 bacterial reference genomes with a minimum length of 500'000 bp, retrieved from the NCBI Reference Sequence Database (date of download: 2020-04-02).

Immunohistochemistry

Immunohistochemical analyses for CD3, CD4, CD8, CD15, CD20, CD68, CD123, CD163, PD-1, MPO, p53, Ki67, C3d and C5b-9 were performed on all lung tissue blocks used in this study. Antibodies, staining protocols and conditions are detailed in **Supplementary Table 4**.

Qualitative and semiquantitative assessment of histopathological lung damage and neutrophilic infiltration

Hematoxylin and eosin (H&E) and Elastica van Gieson (EvG) stained sections of all lung tissues used in this study were independently evaluated by two experienced and board certified pathologists (VZ and KDM) (**Supplementary Table 5**). Both pathologists evaluated the presence of diffuse alveolar damage (DAD), and if present, its stage, intra-alveolar edema and hemorrhage. The characteristic three phases or stages of DAD - exudative (1), proliferative / organizing (2), fibrotic (3) - were assessed as described³⁹. In our cohort of COVID-19 lungs, we observed only DAD stages 1 and/or 2, and the fibrotic phase (3) was not observed. In addition, both pathologists evaluated the severity of histopathological changes in COVID-19 lungs (1 = mild / discrete alterations, 2 = moderate, 3 = severe changes) based on resemblance between normal and pathologically altered lung tissues. Parameters that were taken into account included reduction of alveolar air-filled spaces, typical histologic features of DAD with hyaline membrane formation, infiltration of lymphocytes, monocytes and neutrophils into interstitial and alveolar spaces, type 2 pneumocyte hyperplasia, desquamation of pneumocytes, histologic features of organizing pneumonia including intra-alveolar fibrin deposition and fibrosis (acute fibrinous and organizing pneumonia, AFOP)^{40,41}. The number of neutrophils per lung tissue section was estimated on H&E stained sections and by immunohistochemical stains for CD15 and MPO using a three tiered system (1 = few or no neutrophils, 2 = moderate number of neutrophils, 3 = high number of neutrophils). Assessment of the two pathologists was concordant in the vast majority of cases. Discrepant cases were reviewed by a third pathologist (NW) to reach consent.

Digital image analysis

Slides were digitalized on a 3DHistech™ P1000 slide scanner at 400x magnification (3DHISTECH Ltd. Budapest, Hungary). Digital slide review and quality control was performed by a board-certified pathologist (VHK). Tissue regions with staining artefacts, folds or other technical artefacts were excluded from analysis. A deep neural network (DNN) algorithm (Simoyan and Zisserman VGG, HALO AI™ on HALO™ 3.0.311.167, Indica Labs, Corrales, NM) was trained using pathologist

annotations to automatically localize and measure the area of each lung tissue sample on the digital slides. Background regions and glass were excluded from analysis. Mark-up images for tissue classification were generated and classification accuracy was confirmed through pathology review. For cell-level analysis, color deconvolution for DAB, AP and hematoxylin channels was performed and nuclear segmentation was optimized using cell-morphometric parameters. Marker-positive cells in stromal and epithelial regions were quantified. For CD3, CD4, CD8, CD20, CD68, CD123, CD163 and PD1, staining detection was optimized for the cytoplasmic / membranous compartment and marker expression was measured on a continuous scale at single cell resolution. For assessment of CD8/PD1 double stains, color deconvolution was optimized for separation of DAB (PD1) and AP (CD8) staining products. Internal controls (non-immune cells) and external controls (tonsil) were used to calibrate the detection limits and cross-validated by visual review. For each tissue sample, the total area of lung tissue in mm², the absolute number of marker-positive cells, cell morphometric parameters and staining intensity were recorded.

Identification of SARS-CoV-2 immune response pattern

Gene expression analysis

Samples were included in the study based on quality of libraries and alignment performance. Applied inclusion criteria are: >1 million of mapped reads, good concentration of libraries, average read length >100bp, > 300 target genes with more than 10 reads. One sample with > 1 Mio reads was excluded from the study because of shorter read length and a low library concentration. Notably this sample had the longest time between death and autopsy (72h) before analysis. Differential expression analysis was performed using the edgeR package comparing normal lung samples, COVID-19 samples and samples from patients with other infections. Genes were selected for downstream analyses by $fdr < 0.05$ and $|\logFC| > 1$ for clustering analysis. Clustering analysis was performed using k-means algorithm and complete linkage. Ideal number of clusters ($n=3$) was chosen based on 30 different algorithms⁴² and the final clustering derives from the consensus of 2000 iterations. Expression of gene signatures was calculated as median of $\log_2(\text{cpm} + 1)$ of selected genes.

Functional enrichment analysis

Biological processes enrichment was performed using the enrichGO function of the package clusterProfiler⁴³ setting all the genes included in the assay as universe.

Statistical analysis

All the analyses and graphical representations were performed using the R statistical environment software⁴⁴ and the following packages: ggplot2⁴⁵, circlize⁴⁶, ComplexHeatmap⁴⁷, ggfortify⁴⁸, reshape2⁴⁹ and factoextra⁵⁰. Correlation between transcripts and viral counts was performed using Pearson's correlation. Association between continuous and categorical data were tested using Wilcoxon rank sum test.

Based on the often non-uniform histopathological appearance of lung samples from the same patient, transcriptomic, morphologic or histopathological analyses were performed at the tissue sample level. Analyses involving patients' clinical or demographical data were performed at the patient level, and patients in which all analyzed lung samples expressed an ISG^{high} or an ISG^{low} profile were called ISG^{high} or ISG^{low} patients.

Box-plots elements indicate the median (center line), upper and lower quartiles (box limits) and show all the data points. Whiskers extend to the most extreme value included in 1.5x interquartile range.

Figure Legends

Figure 1. ISG^{high} and ISG^{low} are two gene expression profiles in COVID-19 autopsy lungs

(a) Heatmap showing K-means clustering of COVID-19 and normal lung samples based on expression levels of deregulated genes in COVID-19 versus normal lungs. (b) Comparison of up- and down-regulated genes in lung samples from COVID-19 patients, normal lung samples and samples from other infectious lung pathologies. (c) Principal component analysis (PCA) of COVID-19 and non-COVID-19 lung samples reveals segregation in two distinct groups based on diagnosis and viral load. (d) ISG signature expression in clusters 1 and 2 of COVID-19 lungs defines two profiles of COVID-19 autopsy lungs termed ISG^{high} and ISG^{low}. Study patients with unambiguous sample segregation in either Cluster 1 or 2 were assigned the corresponding ISG activation label ISG^{high} and ISG^{low}, respectively. (e) Hospitalization time in ISG^{high} patients versus ISG^{low} patients. ISG^{high} samples, red; ISG^{low} samples, blue

Figure 2. Co-infections in COVID-19 lungs identified by WGS metagenomics.

No differences in co-infections in ISG^{high} and ISG^{low} COVID-19 lungs identified by WGS metagenomics. (a) Total number of reads generated for each sample. (b) Percentage of reads and (c) absolute numbers of reads not mapping to the human genome (GRCh37 hg19). (d) Bacterial and (e) viral co-infections across lung samples, WGS metagenomic analysis. Purple dots, numbers of reads sufficient for identification of non-human species. Samples are ordered by increasing SARS-CoV-2 viral load in both the ISG^{low} and the ISG^{high} group. Stacked bars, relative abundance of the most common species. Grey bars represent frequent species, colored bars show pathogenic species. *One COVID-19 patient (C3) clustered in the normal control group. ISG^{high} samples, red; ISG^{low} samples, blue

Figure 3. Virological and cellular characteristics of the ISG^{high} and ISG^{low} COVID-19 lung profiles

(a) Correlation of viral load and ISG expression in COVID-19 lungs. Solid lines, sample data from the same patient. Dotted line, regression for all samples. Grey, 95% CI (Pearson's correlation=0.83, adjusted R-squared=0.68, p-value=1.66e-08). (b) Representative immunohistochemistry for SARS-CoV-2 on ISG^{high} and ISG^{low} COVID-19 lung samples and controls. Size bar 100 μ m. (c) Frequencies of immune cells on ISG^{high} and ISG^{low} COVID-19 lung sections and controls. (d) Representative H&E stains and immunohistochemistry (CD3, CD8, CD68, CD163) of ISG^{high} and ISG^{low} COVID-19 lungs and controls, size bar 500 μ m. ISG^{high} samples, red; ISG^{low} samples, blue

Figure 4. Immune cell infiltrates on COVID-19 lung sections.

(a) Frequencies of immune cells on ISG^{high} and ISG^{low} COVID-19 lung sections and controls. (b) Representative immunohistochemistry (CD4, CD20, CD123, CD8/PD1) of ISG^{high} and ISG^{low} COVID-19 lungs and controls, size bar 500 μ m. ISG^{high} samples, red; ISG^{low} samples, blue

Figure 5. Correlation of ISG^{high} and ISG^{low} lung immunoprofiles with morphological changes

(a) Expression of a cytokine signature (TNF, IL-1B, IL6, IFNA17, IFNB1, CCL2, CXCL9, CXCL10, CXCL11) in ISG^{high} and ISG^{low} COVID-19 lung samples. This pro-inflammatory cytokine signature was significantly enriched in the ISG^{high} subset. (b) Inverse correlation of viral load and activated CD8+ T cell signature (CD38, GZMA, GZMB, CCR5). Solid lines, sample data from the same patient. Dotted line, regression for all the samples. Grey, 95% CI (Pearson's correlation=-0.5, adjusted R-squared=0.22, p-value=0.005). (c) Association of DAD stage with ISG expression. (d) Association of the pro-inflammatory cytokine signature with intraalveolar hemorrhage (IAH). (e) Pearson's correlation of pro-inflammatory cytokines in the cytokine signature indicates presence of co-regulated cytokines. (f-i) Association of cytokine signatures in ISG^{high} and ISG^{low} COVID-19 lung samples with IAH. Association of: (f) Median IL6, TNF, IL1B expression (g) Median IFNA17, IFNB1 expression (h) Median CCL2 expression (i) Median CXCL9/10/11 expression in ISG^{high} and ISG^{low} COVID-19 lung samples versus IAH. Only the CXCL9/10/11 sub-signature was positively associated with IAH. (j) Association of CD68+ macrophage infiltrates with DAD. (k) Association of DAD stage with activated CD8+ T cell signature, (l) with CD8+ T cell counts. (m-p) Association of cytokine signatures in ISG^{high} and ISG^{low} COVID-19 lung samples with DAD stage. Association of: (m) Median IL6, TNF, IL1B expression (n) Median IFNA17, IFNB1 expression (o) Median CCL2 expression (p) Median CXCL9/10/11 expression in ISG^{high} and ISG^{low} COVID-19 lung tissue with DAD stage. ISG^{high} samples, red; ISG^{low} samples, blue

Figure 6. Molecular characteristics of the ISG^{high} and ISG^{low} COVID-19 lung profiles

(a) Representative immunohistochemistry for p53 and Ki67. Size bar 100 μ m. (b) Expression of C1QA and C1QB in ISG^{high} and ISG^{low} lung samples. (c) Representative IHC stainings for complement activation products C5b-9 and C3d in ISG^{high}, ISG^{low} COVID-19 and normal control lungs. Size bar 100 μ m. ISG^{high} samples, red; ISG^{low} samples, blue

References

1. Hopkins, J. Corona virus resource center. Latest update: 05/22/2020): <https://coronavirus.jhu.edu/data> (2020).
2. Wu, Z. & McGoogan, J.M. Characteristics of and Important Lessons From the Coronavirus Disease 2019 (COVID-19) Outbreak in China: Summary of a Report of 72314 Cases From the Chinese Center for Disease Control and Prevention. *JAMA* (2020).
3. Chen, G., et al. Clinical and immunological features of severe and moderate coronavirus disease 2019. *J Clin Invest* 130, 2620-2629 (2020).
4. Liao, M., et al. Single-cell landscape of bronchoalveolar immune cells in patients with COVID-19. *Nat Med* 26, 842-844 (2020).
5. Vabret, N., et al. Immunology of COVID-19: Current State of the Science. *Immunity* 52, 910-941 (2020).
6. Menter, T., et al. Post-mortem examination of COVID19 patients reveals diffuse alveolar damage with severe capillary congestion and variegated findings of lungs and other organs suggesting vascular dysfunction. *Histopathology* (2020).
7. Charrad, M., Ghazzali, N., Boiteau, V. & Niknafs, A. NbClust Package: finding the relevant number of clusters in a dataset. *J. Stat. Softw* (2012).
8. Blanco-Melo, D., et al. Imbalanced Host Response to SARS-CoV-2 Drives Development of COVID-19. *Cell* 181, 1036-1045 e1039 (2020).
9. Yan, Q., et al. Longitudinal peripheral blood transcriptional analysis of COVID-19 patients captures disease progression and reveals potential biomarkers. *medRxiv* (2020).
10. Lieberman, N.A.P., et al. In vivo antiviral host response to SARS-CoV-2 by viral load, sex, and age. *bioRxiv* (2020).
11. Zhang, D., et al. COVID-19 infection induces readily detectable morphological and inflammation-related phenotypic changes in peripheral blood monocytes, the severity of which correlate with patient outcome. *medRxiv* (2020).
12. Huang, C., et al. Clinical features of patients infected with 2019 novel coronavirus in Wuhan, China. *Lancet* 395, 497-506 (2020).
13. Wilk, A.J., et al. A single-cell atlas of the peripheral immune response in patients with severe COVID-19. *Nat Med* (2020).
14. Cupovic, J., et al. Central Nervous System Stromal Cells Control Local CD8(+) T Cell Responses during Virus-Induced Neuroinflammation. *Immunity* 44, 622-633 (2016).
15. Channappanavar, R., et al. Dysregulated Type I Interferon and Inflammatory Monocyte-Macrophage Responses Cause Lethal Pneumonia in SARS-CoV-Infected Mice. *Cell Host Microbe* 19, 181-193 (2016).
16. Bodnar, R.J., Yates, C.C., Rodgers, M.E., Du, X. & Wells, A. IP-10 induces dissociation of newly formed blood vessels. *Journal of cell science* 122, 2064-2077 (2009).
17. Yang, Y., et al. Exuberant elevation of IP-10, MCP-3 and IL-1ra during SARS-CoV-2 infection is associated with disease severity and fatal outcome. *medRxiv* 2002, 2020 (2020).
18. Hueso, L., et al. Upregulation of angiostatic chemokines IP-10/CXCL10 and I-TAC/CXCL11 in human obesity and their implication for adipose tissue angiogenesis. *Int J Obes (Lond)* 42, 1406-1417 (2018).
19. Bonfante, H.L., et al. CCL2, CXCL8, CXCL9 and CXCL10 serum levels increase with age but are not altered by treatment with hydroxychloroquine in patients with osteoarthritis of the knees. *Int J Rheum Dis* 20, 1958-1964 (2017).
20. Merad, M. & Martin, J.C. Pathological inflammation in patients with COVID-19: a key role for monocytes and macrophages. *Nat Rev Immunol* 20, 355-362 (2020).
21. Puthusseri, B., et al. Regulation of p53-mediated changes in the uPA-fibrinolytic system and in lung injury by loss of surfactant protein C expression in alveolar epithelial cells. *Am J Physiol Lung Cell Mol Physiol* 312, L783-L796 (2017).
22. Ling, G.S., et al. C1q restrains autoimmunity and viral infection by regulating CD8(+) T cell metabolism. *Science* 360, 558-563 (2018).

23. Diao, B., et al. Reduction and Functional Exhaustion of T Cells in Patients With Coronavirus Disease 2019 (COVID-19). *Front Immunol* 11, 827 (2020).
24. Salje, H., et al. Estimating the burden of SARS-CoV-2 in France. *Science* 369, 208-211 (2020).
25. Bosmuller, H., et al. The evolution of pulmonary pathology in fatal COVID-19 disease: an autopsy study with clinical correlation. *Virchows Arch*, 1-9 (2020).
26. Cervantes-Barragan, L., et al. Control of coronavirus infection through plasmacytoid dendritic-cell-derived type I interferon. *Blood* 109, 1131-1137 (2007).
27. Kindler, E. & Thiel, V. To sense or not to sense viral RNA--essentials of coronavirus innate immune evasion. *Curr Opin Microbiol* 20, 69-75 (2014).
28. Cameron, M.J., et al. Interferon-mediated immunopathological events are associated with atypical innate and adaptive immune responses in patients with severe acute respiratory syndrome. *J Virol* 81, 8692-8706 (2007).
29. Ziegler, C.G.K., et al. SARS-CoV-2 Receptor ACE2 Is an Interferon-Stimulated Gene in Human Airway Epithelial Cells and Is Detected in Specific Cell Subsets across Tissues. *Cell* 181, 1016-1035 e1019 (2020).
30. Hadjadj, J., et al. Impaired type I interferon activity and exacerbated inflammatory responses in severe Covid-19 patients. *MedRxiv* (2020).
31. Konopka, K.E., et al. Diffuse Alveolar Damage (DAD) from Coronavirus Disease 2019 Infection is Morphologically Indistinguishable from Other Causes of DAD. *Histopathology* (2020).
32. Fei, J., et al. Reduction of lymphocyte at early stage elevates severity and death risk of COVID-19 patients: a hospital-based case-cohort study. *medRxiv* (2020).
33. Zheng, M., et al. Functional exhaustion of antiviral lymphocytes in COVID-19 patients. *Cell Mol Immunol* 17, 533-535 (2020).
34. Zhao, J., Zhao, J. & Perlman, S. T cell responses are required for protection from clinical disease and for virus clearance in severe acute respiratory syndrome coronavirus-infected mice. *J Virol* 84, 9318-9325 (2010).
35. Ng, O.W., et al. Memory T cell responses targeting the SARS coronavirus persist up to 11 years post-infection. *Vaccine* 34, 2008-2014 (2016).
36. Wolfel, R., et al. Virological assessment of hospitalized patients with COVID-2019. *Nature* 581, 465-469 (2020).
37. Magro, C., et al. Complement associated microvascular injury and thrombosis in the pathogenesis of severe COVID-19 infection: A report of five cases. *Transl Res* 220, 1-13 (2020).
38. Cugno, M., et al. Complement activation in patients with COVID-19: A novel therapeutic target. *J Allergy Clin Immunol* 146, 215-217 (2020).
39. Sweeney, R.M. & McAuley, D.F. Acute respiratory distress syndrome. *Lancet* 388, 2416-2430 (2016).
40. Copin, M.C., et al. Time to consider histologic pattern of lung injury to treat critically ill patients with COVID-19 infection. *Intensive Care Med* 46, 1124-1126 (2020).
41. Xu, Z., et al. Pathological findings of COVID-19 associated with acute respiratory distress syndrome. *Lancet Respir Med* 8, 420-422 (2020).
42. Bates, D., Mächler, M., Bolker, B. & Walker, S. Fitting linear mixed-effects models using lme4. *arXiv preprint arXiv:1406.5823* (2014).
43. Chikina, M., Robinson, J.D. & Clark, N.L. Hundreds of Genes Experienced Convergent Shifts in Selective Pressure in Marine Mammals. *Mol Biol Evol* 33, 2182-2192 (2016).
44. Team, R.C. R: A language and environment for statistical computing. (2013).
45. Wickham, H. *ggplot2: elegant graphics for data analysis*, (Springer, 2016).
46. Gu, Z., Gu, L., Eils, R., Schlesner, M. & Brors, B. circlize Implements and enhances circular visualization in R. *Bioinformatics* 30, 2811-2812 (2014).
47. Gu, Z., Eils, R. & Schlesner, M. Complex heatmaps reveal patterns and correlations in multidimensional genomic data. *Bioinformatics* 32, 2847-2849 (2016).

48. Horikoshi, M. & Tang, Y. ggfortify: Data visualization tools for statistical analysis results. v0. 1.0. URL <http://CRAN.R-project.org/package=ggfortify>. R package version 0.4 1, 28 (2018).
49. Wickham, H. Reshaping data with the reshape package. *Journal of statistical software* 21, 1-20 (2007).
50. Kassambara, A. & Mundt, F. Package 'factoextra'. Extract and visualize the results of multivariate data analyses 76(2017).

Data availability

The datasets generated and analysed within this study can be accessed in GEO (GSE151764) and are available from the corresponding author upon request.

Acknowledgements

VHK gratefully acknowledges funding by the Promedica Foundation (F-87701-41-01). AT, JDH, TM and KDM are supported by and gratefully acknowledge the Botnar Research Centre for Child Health. We would like to thank Christian Tosch, Beat Béni, Daniel Turek, Melanie Sachs, Anne Graber, Christina Herz, Arbeneshe Berisha, Norbert Wey and the USZ pathology IT team, André Fitsche, Marcel Glönkler, Christiane Mittman and the USZ pathology laboratory team for expert technical support and scanning of slides.

Author contributions

RN, YC, VHK, FD, TJ and KDM jointly conceived the study, performed data interpretation and prepared the manuscript. AT, MB, HM, MT and CA provided intellectual input, provided critical resources and critically reviewed the manuscript. RN, YC, VHK, MH, TH and TJ performed bioinformatic and statistical analysis. AT, JDH, TM, NS, AF collected autopsy specimens, patient data and performed experiments. VZ, NW, WK and CA performed histomorphological evaluation.

All authors approved the final manuscript.

Competing interests

VHK has served as an invited speaker on behalf of Indica Labs. TH and TJ are employees of Novartis. The other authors declare no competing interests.

Table 1a. Clinical Data, COVID-19 cohort (16 patients)

Characteristics	N or x	% or range
Time between symptoms and death	7,4 d	0 - 20 d
Hospitalisation	5,6 d	0 - 13 d
Postmortem interval	28,4 h	11 - 67 h
Age	75 y	53 - 96 y
Sex	M 13 : F 3	
Comorbidities		
Hypertension	16	100 %
Cardiovascular disease	11	68 %
(Pre-)Adipositas	12	75 %
Diabetes	6	37,5 %
Initial clinical presentation		
Cough	13	81,25 %
Fever	12	75 %
Dyspnea	6	37,5 %
Renal failure	6	37,5 %
Laboratory results		
Interleukin-6 (IL6)	5774,72 ng/l	159,00 - 35.152,00 ng/l
C-reactive protein (CRP)	216,36 mg/l	36,00 - 512,00 mg/l
Ferritin	18.037,71 µg/l	1.025,00 - 228.225,00 µg/l
Procalcitonin (PCT)	1.996,92 µg/l	0,47 - 5.300,00 µg/l
Lactate dehydrogenase (LDH)	870,42 U/l	256,00 - 5.267,00 U/l
Troponin T (cTnT)	54,65 ng/l	2,07 - 126,00 ng/l
Treatment		
Hydroxychloroquine	10	62,5 %
Lopinavir/Ritonavir	5	31,25 %

Antibiotics	12	75 %
ACTEMRA (Tocilizumab)	5	31,25 %

Listed laboratory results correspond to the highest (LDH, cTnT), latest (IL6, ferritin, PCT) or last value before administration of ACTEMRA/Tocilizumab (CRP).

Table 1b. Clinical Data, Control cohort (6 patients)

Characteristics	N or x	% or range
Postmortem interval	31,4 h	25 - 46 h
Age	81,3 y	63 - 104 y
Sex	M 5 : F 1	

Table 1c. Clinical Data, Cohort of patients with other infections (4 patients)

Characteristics	N or x	% or range
Postmortem interval	31,5 h	12 - 79 h
Age	79,5 y	58 - 81 y
Sex	M 2 : F 2	

Patients were suffering from other infections of the lung (bacterial or viral pneumonia). Detailed analysis of individual pathogens is shown in Figure 2.

Table 2. Gene ontology enrichment analysis of genes upregulated in COVID-19 samples.

ID	Description	GeneRatio	BgRatio	pvalue	p.adjust
GO:0034340	response to type I interferon	17/66	30/379	3,70E-07	0,000158
GO:0060337	type I interferon signaling pathway	17/66	30/379	3,70E-07	0,000158
GO:0071357	cellular response to type I interferon	17/66	30/379	3,70E-07	0,000158
GO:0051607	defense response to virus	21/66	44/379	5,53E-07	0,000177
GO:0098542	defense response to other organism	25/66	71/379	3,85E-05	0,009888
GO:0009615	response to virus	21/66	57/379	9,79E-05	0,020960
GO:0045069	regulation of viral genome replication	10/66	18/379	1,87E-04	0,034381
GO:1903900	regulation of viral life cycle	11/66	22/379	2,95E-04	0,042931
GO:0045071	negative regulation of viral genome replication	8/66	13/379	3,57E-04	0,042931
GO:1903901	negative regulation of viral life cycle	8/66	13/379	3,57E-04	0,042931
GO:0048525	negative regulation of viral process	9/66	16/379	3,68E-04	0,042931
GO:0051603	proteolysis involved in cellular protein catabolic process	7/66	11/379	6,71E-04	0,071789
GO:0050792	regulation of viral process	12/66	28/379	9,17E-04	0,088399
GO:0019079	viral genome replication	10/66	21/379	9,64E-04	0,088399
GO:0043901	negative regulation of multi-organism process	9/66	18/379	1,16E-03	0,099123

Supplementary Table 2. OIRRA gene list

ABCF1	CCL5	CD40LG	CTAG2	FASLG	HIF1A	IFIT1	IL3RA
ADGRE5	CCNB2	CD44	CTLA4	FCER1G	HLA-A	IFIT2	IL4
ADORA2A	CCR1	CD47	CTSS	FCGR1A	HLA-B	IFIT3	IL6
AIF1	CCR2	CD48	CX3CL1	FCGR2B	HLA-C	IFITM1	IL7
AKT1	CCR4	CD52	CX3CR1	FCGR3A	HLA-DMA	IFITM2	IL7R
ALOX15B	CCR5	CD53	CX3CR1	FCGR3B	HLA-DMB	IFNA17	IRF1
ARG1	CCR6	CD6	CX3CR1	FCRLA	HLA-DOA	IFNB1	IRF4
AXL	CCR7	CD63	CX3CR1	FOXM1	HLA-DOB	IFNG	IRF9
B3GAT1	CD14	CD68	CXCL1	FOXO1	HLA-DPA1	IGF1R	IRS1
BAGE	CD160	CD69	CXCL10	FOXP3	HLA-DPB1	IGSF6	ISG15
BATF	CD163	CD70	CXCL11	FUT4	HLA-DQA1	IKZF1	ISG20
BCL2	CD19	CD74	CXCL13	FYB	HLA-DQA2	IKZF2	ITGA1
BCL2L11	CD1C	CD79A	CXCL8	G6PD	HLA-DQB2	IKZF3	ITGAE
BCL6	CD1D	CD79B	CXCL9	GADD45GIP1	HLA-DRA	IKZF4	ITGAL
BRCA1	CD2	CD80	CXCR2	GAGE1	HLA-DRB1	IL10	ITGAM
BRCA2	CD209	CD83	CXCR3	GAGE10	HLA-E	IL10RA	ITGAX
BST2	CD22	CD86	CXCR4	GAGE12J	HLA-F	IL12A	ITGB1
BTLA	CD226	CD8A	CXCR5	GAGE13	HLA-F-AS1	IL12B	ITGB2
BUB1	CD244	CD8B	CXCR6	GAGE2C	HLA-G	IL13	ITGB7
C10orf54	CD247	CDK1	CYBB	GATA3	HMBS	IL15	ITK
C1QA	CD27	CDKN2A	DDX58	GBP1	ICAM1	IL17A	JAML
C1QB	CD274	CDKN3	DGAT2	GNLY	ICOS	IL17F	JCHAIN
CA4	CD276	CEACAM1	DMBT1	GPR18	ICOSLG	IL18	KIAA0101
CBLB	CD28	CEACAM8	EBI3	GRAP2	ID2	IL1A	KIR2DL1
CCL17	CD33	CIITA	EFNA4	GUSB	ID3	IL1B	KIR2DL2
CCL18	CD37	CLEC4C	EGFR	GZMA	IDO1	IL2	KIR2DL3
CCL2	CD38	CMKLR1	EGR2	GZMB	IDO2	IL21	KLF2
CCL20	CD3D	CORO1A	EGR3	GZMH	IFI27	IL22	KLRB1
CCL21	CD3E	CRTAM	EIF2AK2	GZMK	IFI35	IL23A	KLRD1
CCL22	CD3G	CSF1R	ENTPD1	HAVCR2	IFI44L	IL2RA	KLRF1
CCL3	CD4	CSF2RB	EOMES	HERC6	IFI6	IL2RB	KLRG1
CCL4	CD40	CTAG1B	FAS	HGF	IFIH1	IL2RG	KLRK1

KREMEN1	MLANA	POLR2A	SSX2	TNFSF9
KRT5	MMP2	POU2AF1	STAT1	TOP2A
KRT7	MMP9	PRDM1	STAT3	TP63
LAG3	MPO	PRF1	STAT4	TRIM29
LAMP1	MRC1	PSMB9	STAT5A	TUBB
LAMP3	MS4A1	PTEN	STAT6	TWIST1
LAPTM5	MTOR	PTGS2	TAGAP	TYROBP
LCK	MX1	PTK7	TAP1	VCAM1
LCN2	MYC	PTPN11	TARP	VEGFA
LEXM	NCAM1	PTPN6	TBP	VTCN1
LILRB1	NCF1	PTPN7	TBX21	XAGE1B
LILRB2	NCR1	PTPRC	TCF7	ZAP70
LMNA	NCR3	PTPRCAP	TDO2	ZBTB46
LRG1	NECTIN2	PVR	TFRC	ZEB1
LRP1	NFATC1	PYGL	TGFB1	
LST1	NFKBIA	RB1	TIGIT	
LY9	NKG7	RORC	TLR3	
LYZ	NOS2	RPS6	TLR7	
M6PR	NOTCH3	S100A8	TLR8	
MAD2L1	NRP1	S100A9	TLR9	
MADCAM1	NT5E	SAMHD1	TNF	
MAGEA1	NTN3	SDHA	TNFAIP8	
MAGEA10	OAS1	SELL	TNFRSF14	
MAGEA12	OAS2	SH2D1A	TNFRSF17	
MAGEA3	OAS3	SH2D1B	TNFRSF18	
MAGEA4	PDCD1	SIT1	TNFRSF4	
MAGEC2	PDCD1LG2	SKAP2	TNFRSF9	
MAPK1	PECAM1	SLAMF7	TNFSF10	
MAPK14	PGF	SLAMF8	TNFSF13B	
MELK	PIK3CA	SNAI1	TNFSF14	
MIF	PIK3CD	SNAI2	TNFSF18	
MKI67	PMEL	SRGN	TNFSF4	

Supplementary Table 3. Differentially expressed genes, COVID-19 versus controls

ID	logFC	logCPM	PValue	FDR
DMBT1_64696575	5.086440047	9.507465672	8.27E-12	3.29E-09
TDO2_55162	3.60666041	9.53520997	3.39E-11	6.12E-09
IFI6_47156	3.778639284	14.24783272	4.61E-11	6.12E-09
KIAA0101_319426	3.146999681	8.549063739	8.30E-11	8.26E-09
IGF1R_12291338	-1.346908853	10.50777116	1.63E-10	1.29E-08
MELK_300401	2.899390615	7.833266318	9.68E-10	6.29E-08
BUB1_701803	2.429206201	8.360010662	1.11E-09	6.29E-08
ISG15_66173	4.276622596	13.15626013	1.97E-09	9.78E-08
IFI27_37143	1.911305772	12.5471898	3.00E-09	1.33E-07
PSMB9_384491	1.385731366	10.9106894	6.49E-09	2.58E-07
OAS3_667776	2.754666249	9.890613941	9.75E-09	3.53E-07
CDK1_837939	2.262910126	9.211945164	1.08E-08	3.59E-07
HLA-G_483585	4.030812546	6.375748944	1.47E-08	4.35E-07
SLAMF8_9071016	2.293400189	9.725983998	1.53E-08	4.35E-07
MLANA_159265	-5.75771358	0.738276085	1.83E-08	4.86E-07
CDKN3_434534	1.939803243	8.894315977	2.32E-08	5.46E-07
OAS1_757865	2.607400402	11.38534225	2.33E-08	5.46E-07
JAML_78188	-1.759772394	7.103911839	6.73E-08	1.49E-06
IRS1_37283828	-1.354465089	10.24560172	7.98E-08	1.62E-06
OAS2_15981707	2.021713176	10.70108718	8.12E-08	1.62E-06
CXCL11_261361	4.712702755	12.17691208	8.78E-08	1.66E-06
IDO1_268369	2.77746775	10.21297062	1.32E-07	2.38E-06
FOXM1_10551166	3.511025369	7.302016812	3.85E-07	6.66E-06
LAMP3_12361344	2.218476016	9.184121563	4.93E-07	8.17E-06
IFIT3_72174	2.826535538	12.01665835	6.87E-07	1.07E-05
MAD2L1_115221	1.749064486	8.034765012	7.01E-07	1.07E-05

CD38_519628	1.940842458	9.824900589	7.36E-07	1.08E-05
CCR1_54149	1.473037432	10.11920316	8.34E-07	1.19E-05
GZMB_581688	1.898001877	10.41173908	8.96E-07	1.23E-05
LAG3_13111419	2.386185632	7.994487875	1.01E-06	1.34E-05
TCF7_677799	-1.154491364	6.98289475	1.15E-06	1.48E-05
IFI44L_12771376	2.551619364	11.04872147	1.20E-06	1.49E-05
TOP2A_27522855	2.412862908	9.724530736	1.28E-06	1.55E-05
KLF2_9111017	-1.146655278	10.32922348	1.82E-06	2.13E-05
MX1_232336	2.598359407	11.58716187	2.53E-06	2.88E-05
CXCL9_149250	2.475393657	11.64602422	3.36E-06	3.71E-05
CD276_12011310	1.404468545	6.909158714	3.83E-06	4.12E-05
STAT1_18871996	1.341291438	12.54396256	4.11E-06	4.31E-05
IFI35_419526	1.590766479	9.999010988	4.93E-06	5.03E-05
IFIH1_20172123	1.978276916	9.64184768	5.53E-06	5.50E-05
CCL18_198296	2.559340347	11.50058854	6.63E-06	6.43E-05
KLRB1_177284	-1.356445562	10.32648685	7.21E-06	6.84E-05
CXCR4_100208	-1.262015044	12.69186025	8.67E-06	8.03E-05
GBP1_771872	1.624043959	12.95069926	1.21E-05	0.000109887
CEACAM8_745847	-2.38182276	6.835412175	1.51E-05	0.000133479
IFIT2_124224	2.601872644	12.64896588	1.80E-05	0.000155644
PDCD1LG2_315423	1.435337704	9.765019917	1.94E-05	0.000164473
CXCL10_354459	2.921361689	12.20854003	2.10E-05	0.000173779
IFIT1_158259	3.138880653	12.7962216	2.30E-05	0.000186992
BCL6_21502257	-1.128692675	11.38395943	2.37E-05	0.000188627
CD69_195303	-1.167440855	10.29551815	2.49E-05	0.000194401
PTGS2_14761583	-1.787690656	9.487046641	3.11E-05	0.000229188
CD226_9021006	-1.055303117	8.204262834	3.51E-05	0.000249595
C1QB_111199	1.318021235	14.14106331	5.40E-05	0.000370819

CXCL13_202307	2.634779914	10.17220128	5.53E-05	0.000372978
CCNB2_9861095	2.451586323	8.610014511	6.34E-05	0.000420281
BRCA2_98179922	1.408177984	6.624940626	6.59E-05	0.000429787
MKI67_581686	1.830582251	9.016084457	8.31E-05	0.000533209
BCL2_10401144	-1.054459851	7.084554684	9.27E-05	0.000576492
DDX58_540643	1.637092216	11.5957064	0.000122508	0.000750128
KLRG1_410518	-1.049817337	6.871878081	0.000129441	0.000780569
SNAI2_722828	1.272531289	9.779931728	0.000139876	0.000830906
POU2AF1_230337	1.981866553	9.738343726	0.000172607	0.000967573
XAGE1B_469547	2.99835029	4.93494266	0.000177305	0.000980102
C1QA_67171	1.197339812	12.61310409	0.000183576	0.000989574
PTPRC_710817	-1.011649066	9.527123762	0.000183991	0.000989574
CCL17_288394	-1.834523807	6.992710035	0.0002361	0.001220359
CD1C_12531357	-2.519073627	6.111702351	0.000306038	0.001541811
MPO_15121620	-1.908031327	8.211592408	0.00032134	0.001598665
CCR5_85193	1.040859769	9.653446555	0.00037676	0.001851239
CD83_480580	-1.053864486	8.523628945	0.000393979	0.001889203
CRTAM_312417	-1.623243078	5.490123515	0.000404446	0.001916303
HERC6_17021806	1.846150693	8.504611085	0.000412365	0.001930837
BST2_218322	1.11377782	14.61484839	0.000474995	0.002148274
HLA-DQB2_142243	-2.208546554	2.6772892	0.000635872	0.00275705
CMKLR1_36143	3.089416269	4.095184302	0.000921508	0.003860634
ISG20_642750	1.288727823	10.51232195	0.001035118	0.004203845
TNFSF18_128228	2.048786407	5.115450907	0.001219778	0.004854718
CD163_21422245	1.190748679	13.00811752	0.001277279	0.005033238
CYBB_14221529	1.034200312	11.76129988	0.001416071	0.005525454
IFITM1_359459	1.094499983	14.73592207	0.001527366	0.005845111
RORC_12011307	-1.232621407	6.368975553	0.001648956	0.00625033

TNFRSF9_894998	-1.557976838	6.277732459	0.002060615	0.007593748
IL2_366451	-1.787299469	2.137968085	0.002118414	0.007735127
IRF4_786895	1.2991475	7.589669323	0.002433884	0.008497246
IL21_368450	2.713025334	3.179107785	0.002892483	0.009924208
FCGR1A_547652	1.358837352	8.984718333	0.003056301	0.010396649
SLAMF7_9161020	1.178583741	10.97955754	0.00366687	0.012263986
GZMA_165265	1.05539306	10.51173829	0.004314939	0.014311214
CCR6_271363	-1.108756703	5.421780719	0.004727498	0.015422493
ARG1_174278	-2.016630732	7.856291723	0.005246505	0.016976497
IL10_491598	1.240451265	6.779053894	0.005949936	0.018944598
TNFRSF17_254359	1.607351136	7.694337923	0.006172838	0.019498329
MAGEC2_249358	-2.203350303	-1.572033969	0.007805425	0.024081854
CXCR5_153252	-1.570791614	3.754056017	0.009131323	0.027955897
KRT5_10631165	2.093456369	10.18852794	0.009780171	0.029488696
KRT7_440543	1.017265847	12.56930876	0.012411449	0.035795337
GAGE10_137250	-2.028791387	1.82618068	0.018144659	0.049462838

Supplementary Table 4. Antibodies and staining conditions

Antibody	Supplier	Product Number	Clone	Dilution	Pretreatment	Staining platform	Detection system
CD3	Novocastra	NCL-L-CD3-565	LN10	1:100	H2(20)100	Bond III	Bond Polymer Refine Red Detection (DS9390)
CD4	Novocastra	CD4-368-L-CE	4B12	1:80	30min ER2 95°C	Bond III	Bond Polymer Refine Red Detection (DS9390)
CD8	Novocastra	NCL-L-CD8-4B11	4B11	1:40	H2(30)95	Bond III	Bond Polymer Refine Red Detection (DS9390)
CD15	Cellmarque	115M	MMA	1:25	H1(20)100	Bond III	Bond Polymer Refine Red Detection (DS9390)
CD20	Agilent	M0755	L26	1:600	H2(20)95	Bond III	Bond Polymer Refine Red Detection (DS9390)
CD68	Agilent	M0876	PG-M1	1:100	E1(5)	Bond III	Bond Polymer Refine Red Detection (DS9390)
CD123	Novocastra	CD123-L-CE	BR4MS	1:20	20min ER2 95°C	Bond III	Bond Polymer Refine Red Detection (DS9390)
CD163	Novocastra	NCL-L-CD163	10D6	1:200	H1(20)100	Bond III	Bond Polymer Refine Red Detection (DS9390)
C3d	Dako	A0063	polyclonal	1:700	E1(10)	Bond III	Bond Polymer Refine Red Detection (DS9390)
C5b-9	Lifespan Biosciences		aE11	1:50	Enzyme 1 (5)	Benchmark GX	OptiView DAB (Bestellnummer: 760-700)
Ki67	Agilent	M7240	MIB-1	1:50	H2(20)95	Bond III	Bond Polymer Refine Red Detection (DS9390)
MPO	Agilent	A0398	polyclonal	1:8000	H2(20)95	Bond III	Bond Polymer Refine Red Detection (DS9390)
p53	Agilent	M7001	D07	1:1200	H1(20)100	Bond III	Bond Polymer Refine Red Detection (DS9390)
PD1	Roche Ventana	760-4895	NAT105	no dilution	CC1 40min	Benchmark GX	OptiView DAB (Bestellnummer: 760-700)
SARS-CoV-2	BioConcept	200-401-A50	Anti-SARS-CoV Nucleocapsid	1:6400	H2(20)95	Bond III	Bond Polymer Refine Red Detection (DS9390)

Supplementary Table 5. Histopathology

Case No.	Severity of histological changes in lungs ¹	DAD stage ²	Intraalveolar edema ³	Intraalveolar hemorrhage ³	Neutrophils ⁴	SARS-COV-2 genomes / 10 ⁶ RNaseP copies	SARS-CoV-2 IHC ⁴
C12	1	-	1	1	1	673	1
	2	1	1	1	2	2'871	2
	2	1	1	1	2	116'310	3
C13	3	1 and 2	1	1	2	38	0
	3	1 and 2	1	1	2	310	0
	3	1 and 2	1	1	2	225	0
C16	1	1	1	0	1	91	0
	1	1 and 2	1	0	1	20	0
C17	1	2	1	1	1	12	0
	2	1 and 2	1	1	2	25	0
C19	1	1	1	1	1	7'603	2
	1	1	0	1	1	18'867	2
C20	3	1 and 2	1	1	2	145	0
	2	1 and 2	1	1	2	3'205	1
	3	1 and 2	1	1	2	32	0
C21	3	2	0	0	2	119	0
	3	2	0	0	1	53	0
	2	2	0	0	1	119	0
C15	2	1	1	0	2	91'186	3
	2	1	1	0	1	2'993	2
C1	1	-	1	0	1	0.4	0
	1	-	1	0	1	0.0	0
	1	-	1	0	1	0.2	0
C3	2	-	0	0	3	14'311	n.d.
	2	-	1	1	3	249'937	3
	2	-	0	0	3	157'042	2
C4	1	-	0	1	1	314'728	3
	2	-	1	1	1	245'331	3
	2	1	1	1	1	187'540	3
C5	2	-	0	0	1	8	0
	2	1 and 2	0	0	1	180	0
	2	1 and 2	0	1	2	82	0

C6	1	-	0	0	1	10'451	1
	1	-	0	0	1	118'620	3
	1	-	1	0	1	114'407	3
C7	1	1 and 2	0	0	1	12'939	3
	1	1 and 2	0	0	1	1'443	1
	1	1 and 2	0	1	2	16'534	2
C8	1	-	0	0	1	17'598	n.d.
	3	-	1	0	3	316	n.d.
	1	-	0	0	1	139	n.d.
C9	1	-	0	0	1	64'242	n.d.
	1	-	0	0	1	85'137	n.d.
	1	-	1	0	1	29'487	n.d.

At least two different tissue blocks from different areas of the lungs were evaluated for each case.

¹ 1 = slight to moderate changes; 2 = moderate changes; 3 = severe changes

² 1 = exudative; 2 = proliferative / organizing; 3 = fibrotic

³ 1 = yes; 0 = no

⁴ 1 = very few or few; 2 = moderate; 3 = numerous

Figure 1

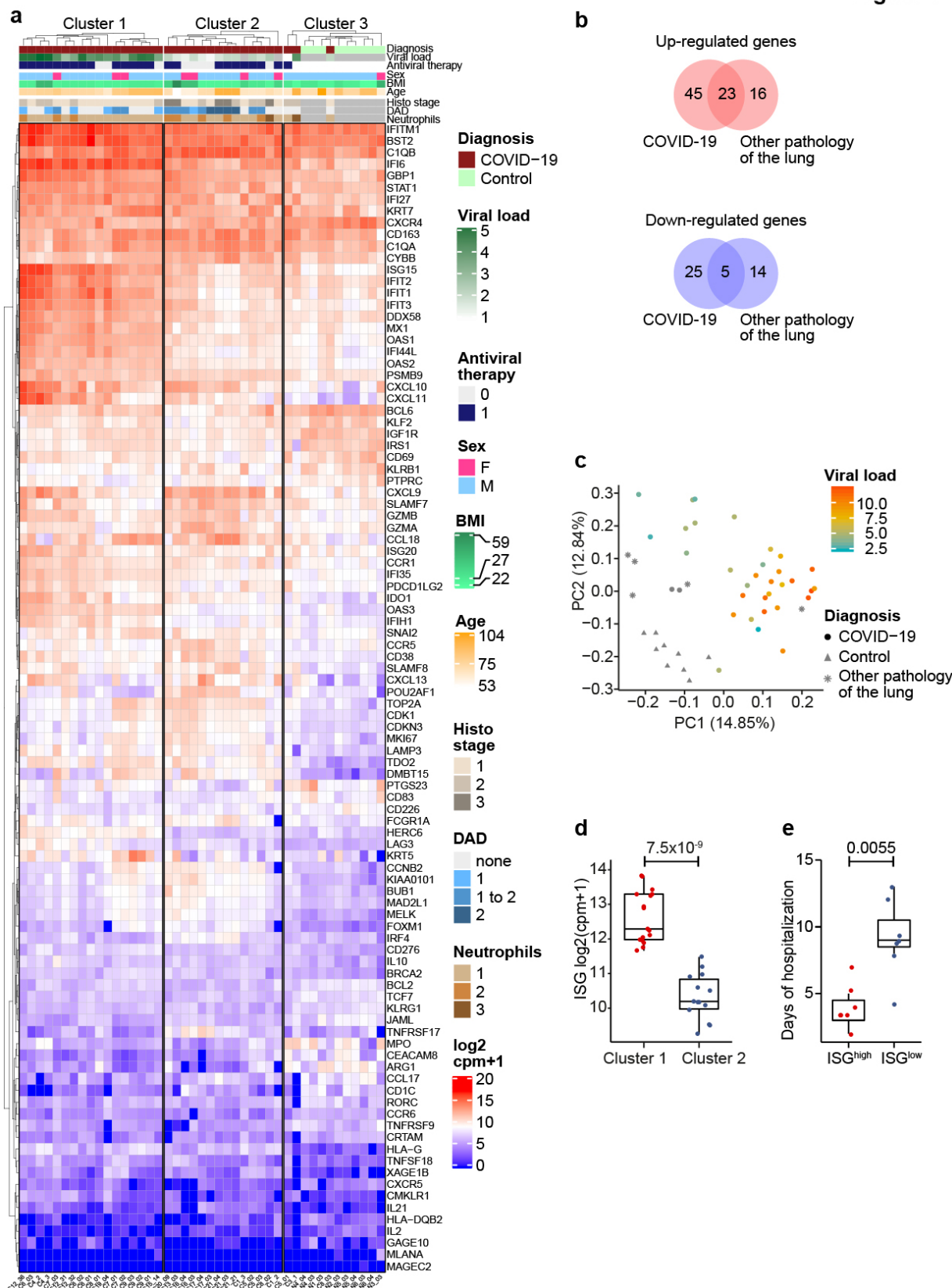


Figure 2

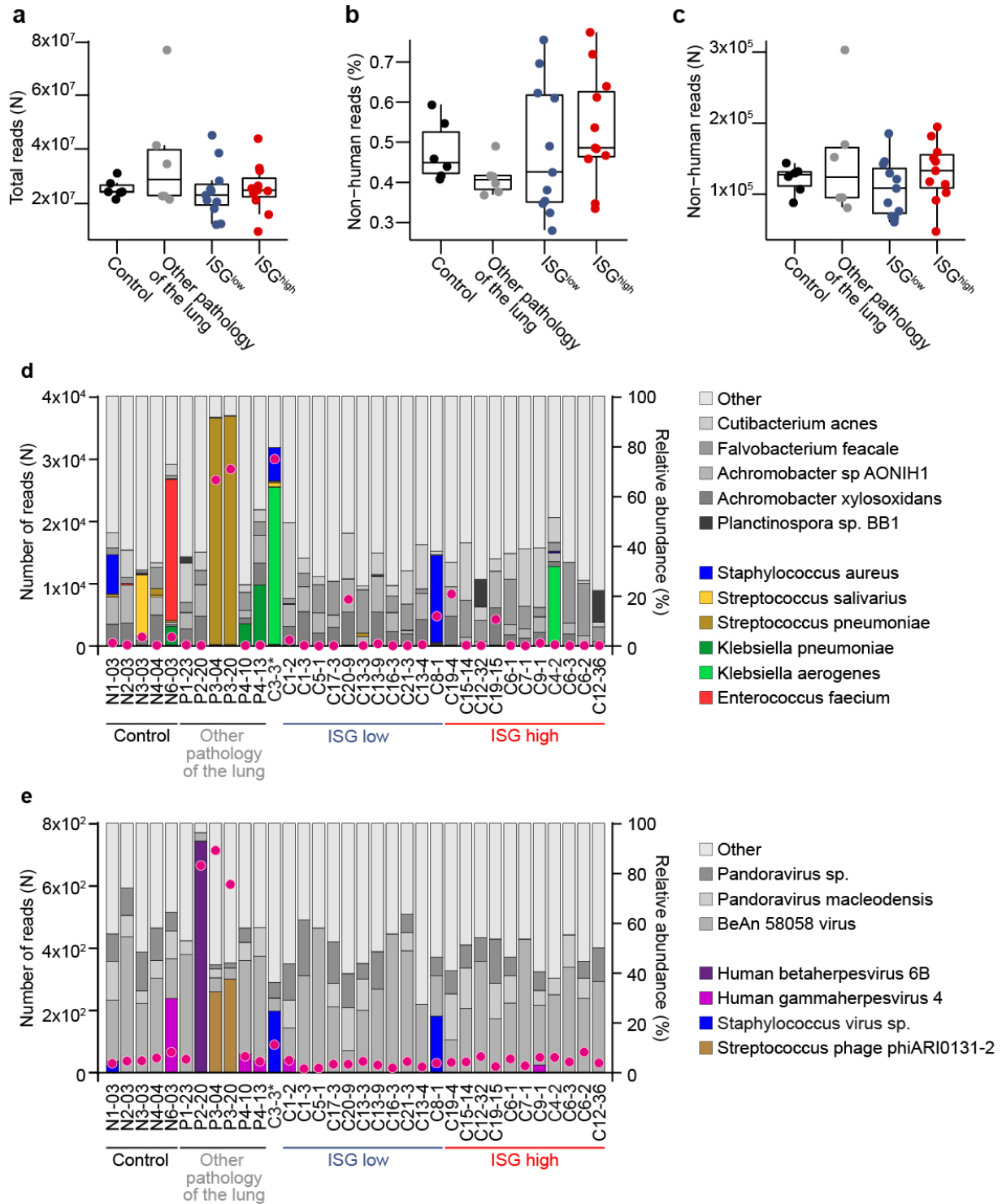


Figure 3

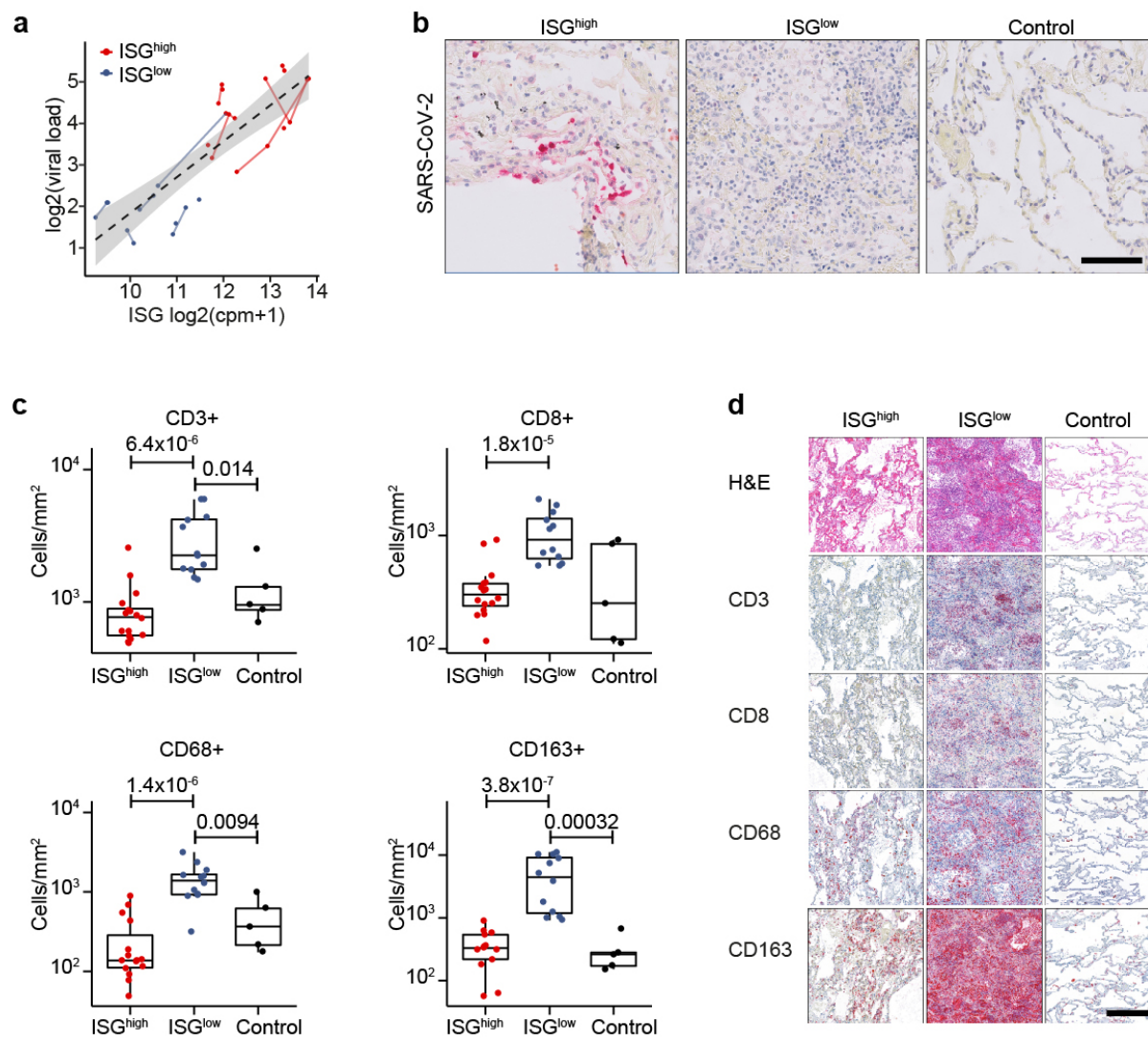


Figure 4

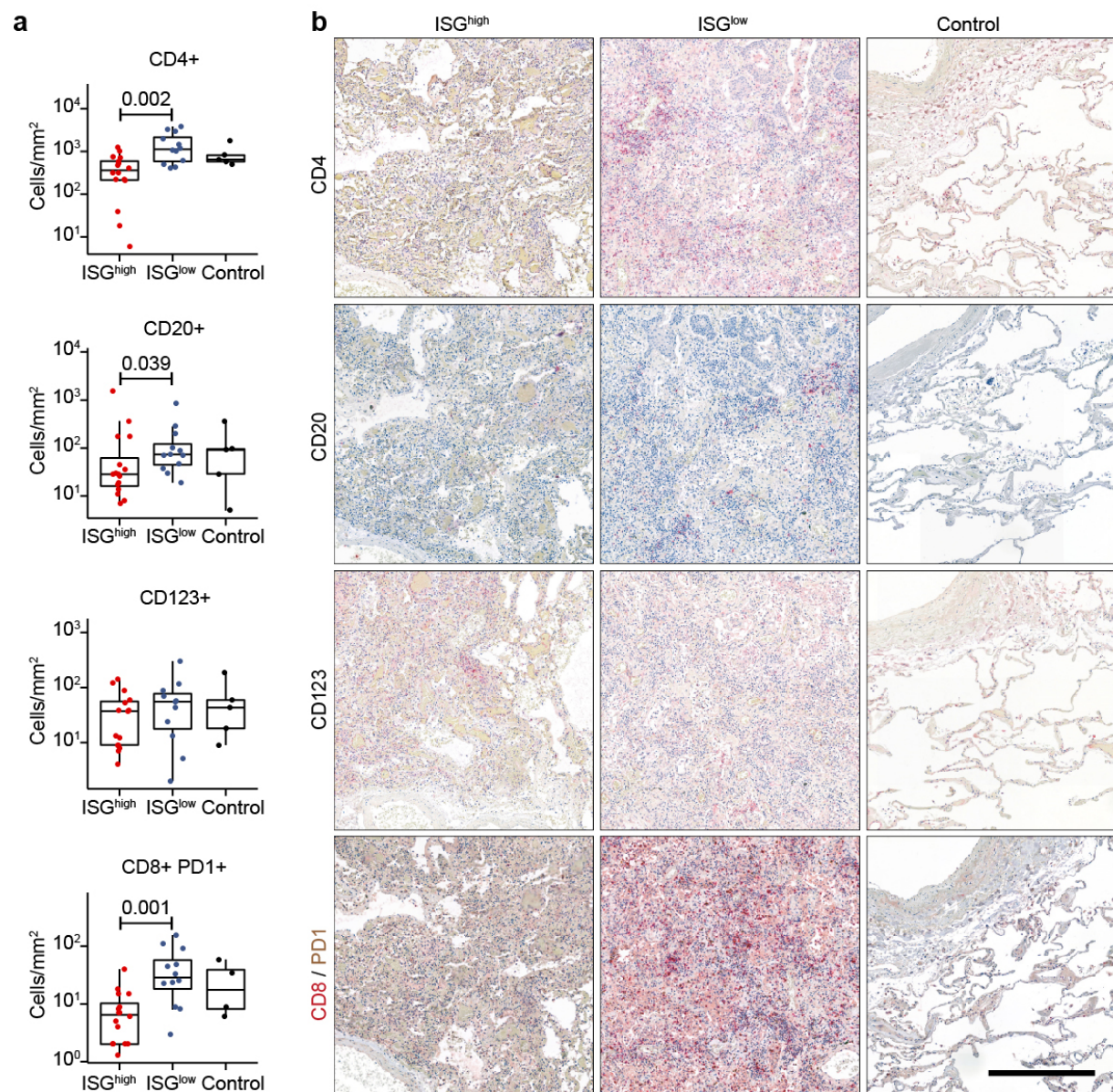


Figure 5

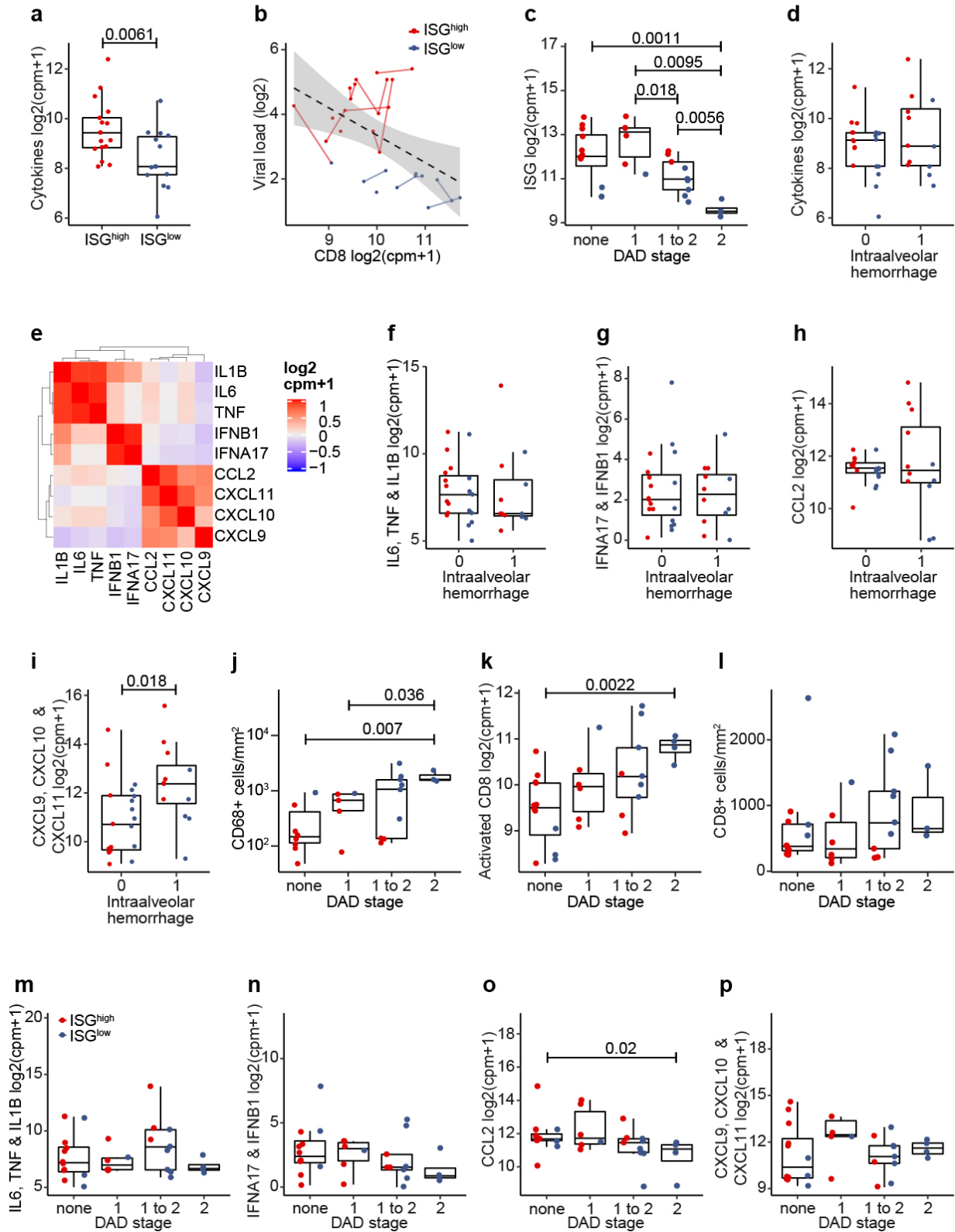


Figure 6

